

COMPARISON AND ERROR MODELING OF VELOCITY INITIAL ORBIT DETERMINATION ALGORITHMS

Linyi Hou *, Kevin Lohan †, and Zachary Putnam ‡

Recently, Christian and Hollenberg proposed and solved a new class of initial orbit determination problems whereby a spacecraft's orbit is determined using only velocity measurements.^{1,2} This paper introduces a modification to the velocity initial orbit determination algorithm that improves both accuracy and computational efficiency. Changes in the orbit determination error with respect to semi-major axis, eccentricity, true anomaly, sensor noise, measurement duration, and number of measurements are then analytically modeled using the orbit hodograph. Finally, the analytic model is compared against Monte Carlo simulations using the improved algorithm. Results show the analytic model accurately predicts changes in orbit determination error.

INTRODUCTION

Initial orbit determination (IOD) refers to the process of determining the orbit of an object in space from a set of measurements, with no a priori knowledge of the orbit itself. IOD is a core problem in astrodynamics and highly relevant to spacecraft navigation. Traditional IOD methods have invariably relied, in some way, on measurements of the object's position. Methods by Laplace, Gauss, and Gooding all require the at least three measurements of the object's angular position.³⁻⁷ Gibbs' method solves the IOD problem with three position vectors.^{5,6} Lambert's method requires two position vectors and the time of flight between those two positions.³

Past IOD methods leveraged measurements from available technology of the time, yet with the development of new sensing techniques, more types of measurement data have become available, calling for the development of novel IOD techniques. Velocity initial orbit determination (VIOD) is a new class of IOD problem recently proposed and solved by Christian and Hollenberg.^{1,2} Their work was inspired by the development of x-ray pulsar navigation (XNAV), a navigation technique based on observing stable millisecond x-ray pulsars. XNAV is notable for its capability to obtain inertial velocity measurements without the need for position information.⁸

A prototype XNAV system was recently demonstrated on-board the International Space Station.⁹⁻¹¹ Whereas vehicles far from Earth typically rely on the Deep Space Network (DSN) to support navigation needs, XNAV is independent from Earth-based systems. Not only does this mean XNAV is not limited by scheduling issues, it also does not suffer from concerns such as reduced accuracy in the transverse directions in the case of the DSN.⁸ XNAV combined with VIOD could become an enabling technology for autonomous deep space navigation.

* Undergraduate Student, Department of Aerospace Engineering, University of Illinois at Urbana-Champaign, Urbana, IL

† Ph.D. Student, Department of Aerospace Engineering, University of Illinois at Urbana-Champaign, Urbana, IL

‡ Assistant Professor, Department of Aerospace Engineering, University of Illinois at Urbana-Champaign, Urbana, IL.

Principally, VIOD relies on the measurement of three or more inertial velocity vectors to determine the orbit of an object by finding corresponding position vectors. In this sense, it can be framed as the inverse of Gibbs' problem. While Christian and Hollenberg have developed two algorithms for solving the VIOD problem,^{1,2} little analysis has been performed to compare and assess these algorithms in terms of accuracy and computational efficiency. Understanding VIOD performance is the first step to determining its utility.

This paper establishes a framework to model VIOD error trends with respect to several mission and sensor parameters using the orbit hodograph. First, an improved VIOD algorithm is proposed and compared against previously developed algorithms. Then, VIOD error trends are analytically modeled. Finally, the model is verified using Monte Carlo simulations. Note that the models presented in this paper are intended only for modeling how VIOD error changes with respect to certain parameters, but does not predict numeric values of VIOD error for any particular set of parameters.

METHODOLOGY

Throughout this paper, Monte Carlo simulations are used to examine VIOD error in the presence of noise. In this section, the underlying orbit simulation and sensor noise models are outlined, along with definitions for canonical units and VIOD error.

Orbit Simulation

A spacecraft in two-body motion is assumed for orbit simulations:

$$\frac{d^2}{dt^2}\mathbf{r} = -\frac{\mu}{\|\mathbf{r}\|^3}\mathbf{r} \quad (1)$$

where \mathbf{r} is the position vector of the spacecraft relative to the central body, and μ is the gravitational parameter of the central body. The spacecraft's position and velocity can then be expressed analytically at any point in the orbit using the Keplerian elements $\{a, e, i, \Omega, \omega, f\}$:

$$\begin{aligned} \mathbf{r} = & r(\cos \Omega \cos \theta - \sin \Omega \sin \theta \cos i)\hat{\mathbf{I}} \\ & + r(\sin \Omega \cos \theta + \cos \Omega \sin \theta \cos i)\hat{\mathbf{J}} \\ & + r \sin \theta \sin i \hat{\mathbf{K}} \end{aligned} \quad (2)$$

$$\begin{aligned} \mathbf{v} = & -\frac{\mu}{h}[\cos \Omega(\sin \theta + e \sin \omega) + \sin \Omega(\cos \theta + e \cos \omega) \cos i]\hat{\mathbf{I}} \\ & -\frac{\mu}{h}[\sin \Omega(\sin \theta + e \sin \omega) - \cos \Omega(\cos \theta + e \cos \omega) \cos i]\hat{\mathbf{J}} \\ & +\frac{\mu}{h}(\cos \theta + e \cos \omega) \sin i \hat{\mathbf{K}} \end{aligned} \quad (3)$$

where $r = \|\mathbf{r}\|$ and h is the specific angular momentum of the spacecraft:

$$r = \frac{a(1 - e^2)}{1 + e \cos f} \quad (4)$$

$$h = \sqrt{\mu a(1 - e^2)} \quad (5)$$

Orbit simulations were performed in MATLAB. The spacecraft orbit is defined using the Keplerian elements, and the spacecraft states \mathbf{r}, \mathbf{v} are propagated analytically using Eqs. (2)-(5) by

propagating the true anomaly f . The true anomaly is found by solving Kepler's equation using Newton's method in Eq. (6), and then solving Eq. (7):

$$M = E - e \sin E \quad (6)$$

$$\tan \frac{E}{2} = \left(\frac{1-e}{1+e} \right)^{1/2} \tan \frac{f}{2} \quad (7)$$

where M is the mean anomaly and E is the eccentric anomaly. To obtain M for a time t since periapsis passage, one simply computes $M = t\sqrt{\mu/a^3}$.

Sensor Noise Modeling

With the position and velocity vectors defined, simulated sensor noise can then be added to the velocity measurements. Sensor noise is modeled by a Gaussian distribution centered at zero with a standard deviation of σ . The sensor noise direction is randomized in 3D space. Given the Gaussian distribution function $\mathcal{N}(\mu, \sigma^2)$ where μ is the mean and σ is the standard deviation, the sensor noise σ_n may be computed as

$$\boldsymbol{\sigma}^* = \mathcal{N}(0, 1)\hat{I} + \mathcal{N}(0, 1)\hat{J} + \mathcal{N}(0, 1)\hat{K} \quad (8)$$

$$\boldsymbol{\sigma}_n = \mathcal{N}(0, \sigma^2) \frac{\boldsymbol{\sigma}^*}{\|\boldsymbol{\sigma}^*\|} \quad (9)$$

subsequently, the noisy velocity measurement $\tilde{\mathbf{v}}$ can be calculated:

$$\tilde{\mathbf{v}} = \mathbf{v} + \boldsymbol{\sigma}_n \quad (10)$$

Canonical Units

Canonical units are used throughout this paper to standardize simulation results. Canonical units were constructed by defining the distance unit, DU , using the semi-major axis:

$$\mu \triangleq 1 \frac{DU^3}{TU^2} \quad , \quad a \triangleq 1 \times 10^5 \text{ } DU \quad (11)$$

where DU is the canonical distance unit, TU is the canonical time unit, a is the semi-major axis, and μ is the gravitational parameter of the central body. It follows that

$$DU = \frac{a}{1 \times 10^5} \quad , \quad TU = \sqrt{\frac{DU^3}{\mu}} \quad (12)$$

Error Evaluation

To assess the accuracy of VIOD algorithms, let ϵ be the relative mean squared error (MSE) between the calculated position from VIOD, $\tilde{\mathbf{r}}$, and the spacecraft's true position in space, \mathbf{r} :

$$\epsilon = \sqrt{\frac{1}{n} \sum_i^n \frac{\|\tilde{\mathbf{r}}_i - \mathbf{r}\|}{\|\mathbf{r}\|}} \quad (13)$$

REVIEW OF VIOD ALGORITHMS

Christian and Hollenberg previously introduced two different VIOD algorithms,^{1,2} which this paper shall refer to as the "energy method" and the "hodograph method". Their solution approaches are outlined in the subsections below. A review of the orbit hodograph is provided. An improved version of the hodograph method is also proposed and outlined.

The Energy Method

The "energy method" proposed by Christian and Hollenberg¹ utilizes the conservation of momentum and the vis-viva equation to construct a linear system and solve the VIOD problem. The solution process is summarized below:

Observe that three given velocity vectors $\{v_1, v_2, v_3\}$ must lie on the same orbital plane. In the presence of noise, a least-squares approach can be used to determine the orbital plane that best fits the velocity vectors. Construct the matrix N :

$$N = [v_1, v_2, v_3]^T \quad (14)$$

The unit vector k orthogonal to the orbital plane can be found by taking the singular value decomposition (SVD) $N = UDV^T$ and selecting the column in V corresponding to the smallest singular value in D . With the orientation of the orbital plane defined, construct Eqs. (15)-(18):

$$u_i = \frac{v_i}{\|v_i\|} \quad , \quad w_i = \frac{u_i \times k}{\|u_i \times k\|} \quad (15)$$

$$r_{u_i} = (u_i u_i^T) r_i \quad , \quad r_{w_i} = (w_i w_i^T) r_i \quad (16)$$

$$h = r \times v \quad , \quad z_i = \frac{1}{\|v_i\|} w_i \quad (17)$$

$$\alpha_i = \frac{\mu}{\|r_i\|} \quad , \quad \beta_i = \gamma_i \frac{\mu}{\|r_i\|} \frac{\|r_{u_i}\|}{\|h\|} \quad (18)$$

where $\gamma_i = \pm 1$ such that $r_{u_i} = \gamma_i \|r_{u_i}\| u_i$. Define the vector g :

$$g = [\alpha_1 \ \beta_1 \ \alpha_2 \ \beta_2 \ \alpha_3 \ \beta_3]^T \quad (19)$$

A linear system may now be constructed:

$$\begin{bmatrix} z_1 & u_1 & -z_2 & -u_2 & \mathbf{0}_{3 \times 1} & \mathbf{0}_{3 \times 1} \\ z_1 & u_1 & \mathbf{0}_{3 \times 1} & \mathbf{0}_{3 \times 1} & -z_3 & -u_3 \\ \mathbf{0}_{3 \times 1} & \mathbf{0}_{3 \times 1} & z_2 & u_2 & -z_3 & -u_3 \\ 1 & 0 & -1 & 0 & 0 & 0 \\ 1 & 0 & 0 & 0 & -1 & 0 \\ 0 & 0 & 1 & 0 & -1 & 0 \end{bmatrix} g = \begin{bmatrix} \|v_1\| w_1 - \|v_2\| w_2 \\ \|v_1\| w_1 - \|v_3\| w_3 \\ \|v_2\| w_2 - \|v_3\| w_3 \\ \|v_1\|^2/2 - \|v_2\|^2/2 \\ \|v_1\|^2/2 - \|v_3\|^2/2 \\ \|v_2\|^2/2 - \|v_3\|^2/2 \end{bmatrix} \quad (20)$$

Solving for \mathbf{g} then leads to the position vector \mathbf{r}_i via Eqs. (21)-(24):

$$\|\mathbf{r}_i\| = \frac{\mu}{\alpha_i} \quad (21)$$

$$\mathbf{r}_{w_i} = h\mathbf{z}_i \quad (22)$$

$$\mathbf{r}_{u_i} = \frac{\beta_i h \|\mathbf{r}_i\|}{\mu} \mathbf{u}_i \quad (23)$$

$$\mathbf{r}_i = \mathbf{r}_{w_i} + \mathbf{r}_{u_i} \quad (24)$$

Further details of the solution process can be found in Reference 1. The linear system shown in Eq. (20) can accommodate more than three measurements by including all unique $\{i, j\}$ pairs and expanding the matrices accordingly.

Review of the Orbit Hodograph

A brief review of the orbit hodograph is provided before the discussion of two other VIOD algorithms based on the hodograph. Consider a spacecraft in orbit about a central body (CB). All velocity vectors measured in orbit can be plotted from the origin to form a circle known as the hodograph. The hodograph has radius R and its center is offset from the origin by c , with $c = eR$ where e is the eccentricity of the orbit. The true anomaly spanned by velocity measurements is Δf .

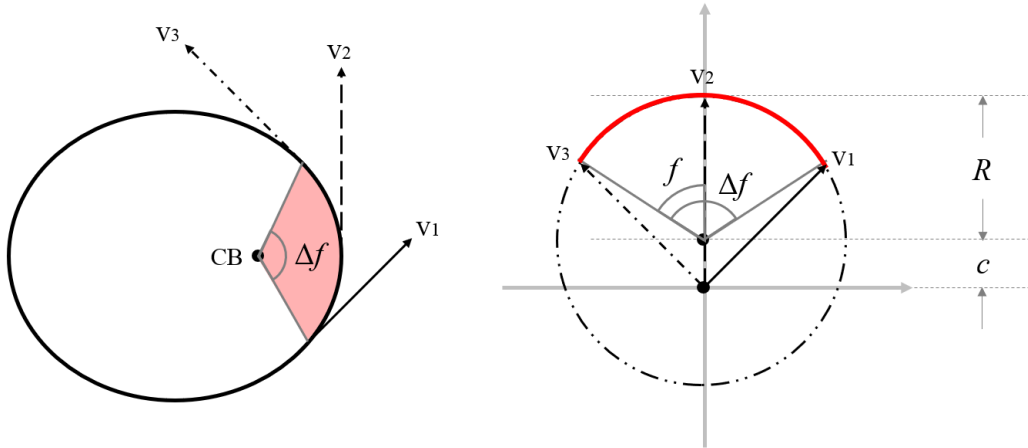


Figure 1. Velocity measurements taken along the orbit are mapped onto the hodograph. Solid ellipse: spacecraft orbit (left). Dot-dash circle: orbit hodograph (right).

The Hodograph Method

The "hodograph method" introduced by Hollenberg and Christian² applies circle fitting to the velocity hodograph to solve the VIOD problem. Their solution is summarized below:

Using the same approach as the energy method, obtain the unit vector \mathbf{k} normal to the orbital plane. Next, define a new reference frame (the "orbital" frame) for the velocity vectors, where the z-axis is aligned with \mathbf{k} , and the x-axis is perpendicular to both \mathbf{v}_1 and \mathbf{k} , as shown in Eq. (25). The

rotation matrix to this new reference frame is given by \mathbf{T}_O^I , defined in Eq. (26).

$$\mathbf{u}_x = \frac{\mathbf{v}_1 \times \mathbf{k}}{\|\mathbf{v}_1 \times \mathbf{k}\|} \quad (25)$$

$$\mathbf{T}_O^I = [\mathbf{u}_x, \mathbf{u}_y, \mathbf{k}]^T \quad (26)$$

Now, the measurements $\{\mathbf{v}_1, \dots, \mathbf{v}_n\}$ can be converted to the orbital frame with Eq. (27). Note that $\dot{z}_{O_i} \approx 0$ when the measurement noise is small.

$$[\dot{x}_{O_i}, \dot{y}_{O_i}, \dot{z}_{O_i}]^T = \mathbf{T}_O^I \mathbf{v}_i \quad (27)$$

Subsequently, a linear system may be constructed as shown by Eq. (28):

$$\begin{bmatrix} 2\dot{x}_{O_1} & 2\dot{y}_{O_1} & 1 \\ \vdots & \vdots & \vdots \\ 2\dot{x}_{O_n} & 2\dot{y}_{O_n} & 1 \end{bmatrix} \begin{bmatrix} \dot{x}_c \\ \dot{y}_c \\ g \end{bmatrix} = \begin{bmatrix} \dot{x}_{O_1}^2 + \dot{y}_{O_1}^2 \\ \vdots \\ \dot{x}_{O_n}^2 + \dot{y}_{O_n}^2 \end{bmatrix} \quad (28)$$

where (\dot{x}_c, \dot{y}_c) is the center of the hodograph, and the hodograph radius can be found using Eq. (29):

$$R = \sqrt{\dot{x}_c^2 + \dot{y}_c^2 - g} \quad (29)$$

The coordinates of the hodograph center and the eccentricity vector in the inertial frame are:

$$\mathbf{c} = [\mathbf{T}_O^I]^T \begin{bmatrix} \dot{x}_c \\ \dot{y}_c \\ 0 \end{bmatrix} \quad (30)$$

$$\mathbf{e} = \frac{\mathbf{c}}{R} \times \mathbf{k} \quad (31)$$

Finally, construct the following vector components

$$\mathbf{u}_{\perp_i} = \frac{\mathbf{v}_i - \mathbf{c}}{\|\mathbf{v}_i - \mathbf{c}\|} \quad (32)$$

$$\mathbf{u}_{\parallel_i} = \frac{\mathbf{v}_i - \mathbf{c}}{\|\mathbf{v}_i - \mathbf{c}\|} \times \mathbf{k} \quad (33)$$

$$\mathbf{v}_{\perp_i} = (\mathbf{u}_{\perp_i} \mathbf{u}_{\perp_i}^T) \mathbf{v}_i \quad (34)$$

which can be assembled into the position vector via Eqs. (35)-(36).

$$\rho_i = \frac{\mu \|\mathbf{e} + \mathbf{u}_{\parallel_i}\|}{\|\mathbf{v}_{\perp_i}\| \|\mathbf{v}_i\|} \quad (35)$$

$$\mathbf{r}_i = \rho_i \mathbf{u}_{\parallel_i} \quad (36)$$

The hodograph method can similarly be extended for more than three measurements by expanding Eq. (28) to accommodate additional data. Further details on the implementation of this algorithm can be found in Reference 2.

The Improved Hodograph Method

This paper proposes an improvement to the hodograph method by using an alternative circle fitting algorithm. The original algorithm in Eq. (28) is a non-iterative algebraic fitting method known as the Kåsa fit. The Kåsa fit produces results biased toward small circles when given data points sampled from short arcs.^{12,13} The accuracy of this process may be improved by using the so-called "hyperaccurate" algebraic fit, an iterative algebraic approach described in Reference 12 which eliminates essential bias to achieve a more accurate fit. The "hyperaccurate" circle fitting algorithm is summarized below as follows:

Define a circle by the algebraic equation

$$A(x^2 + y^2) + Bx + Cy + D = 0. \quad (37)$$

Let $\mathbf{A} = (A, B, C, D)$ be the parameter vector, and define

$$\mathbf{Z} \triangleq \begin{bmatrix} z_1 & x_1 & y_1 & 1 \\ \vdots & \vdots & \vdots & \vdots \\ z_n & x_n & y_n & 1 \end{bmatrix} \quad (38)$$

where $z_i = x_i^2 + y_i^2$. Next, define the "data matrix" as:

$$\mathbf{M} \triangleq \frac{1}{n} \mathbf{Z}^T \mathbf{Z} = \begin{bmatrix} \bar{z}z & \bar{z}x & \bar{z}y & \bar{z} \\ \bar{z}x & \bar{x}x & \bar{x}y & \bar{x} \\ \bar{z}y & \bar{x}y & \bar{y}y & \bar{y} \\ \bar{z} & \bar{x} & \bar{y} & 1 \end{bmatrix} \quad (39)$$

The circle fitting problem becomes a problem of minimizing the equation

$$f(\mathbf{A}) = \mathbf{A}^T \mathbf{M} \mathbf{A}, \quad (40)$$

subject to $\mathbf{A}^T \mathbf{N} \mathbf{A} = 1$, where

$$\mathbf{N} = \begin{bmatrix} 8\bar{z} & 4\bar{x} & 4\bar{y} & 2 \\ 4\bar{x} & 1 & 0 & 0 \\ 4\bar{y} & 0 & 1 & 0 \\ 2 & 0 & 0 & 0 \end{bmatrix} \quad (41)$$

All algebraic circle fitting algorithms can be generalized to this form with different choices of \mathbf{N} . The hyperaccurate fit identifies a choice of \mathbf{N} that yields no essential bias, thus achieving a smaller error overall. The algorithm was implemented in C++ in Reference 14. The algorithm produces the same outputs (\dot{x}_c, \dot{y}_c) and R , which are then used in the same way as shown in Eqs. (30)-(36).

COMPARISON OF VIOD ALGORITHMS

The energy method, hodograph method, and improved hodograph method were compared in the context of both VIOD accuracy and computation time. A 3000-run Monte Carlo sim was performed in MATLAB using an orbit with $\mu = 1$ and Keplerian elements $a = 1 \times 10^5 DU$, $e = 0.5$, $i = \Omega = \omega = 0^\circ$, and $f = 160^\circ$. Twenty (20) measurements are taken over 10% of the orbit period with the sensor noise standard deviation $\sigma = 3 \times 10^{-6} DU/TU$. This equates to measuring in a 7200 km Low Earth Orbit for 10 minutes with a sensor noise standard deviation of 7.1 m/s.

Accuracy

The accuracy of the three VIOD methods were assessed by independently varying either the noise, eccentricity, or starting true anomaly. The results are shown in Figure 2. The improved method becomes notably more accurate than the other two methods when noise or eccentricity increases, or when the measurements start near apoapsis.

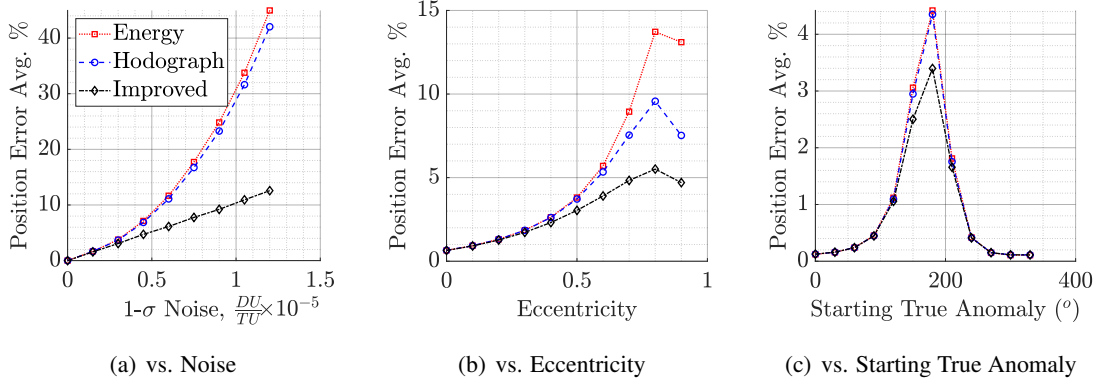


Figure 2. The improved hodograph method outperforms other VIOD methods when noise and/or eccentricity is large, and when measurements are taken near apoapsis.

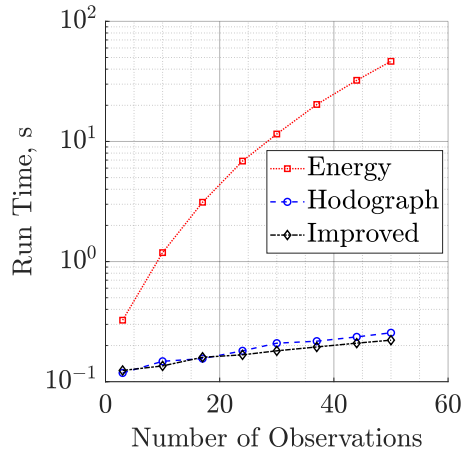


Figure 3. VIOD computation time comparison.

#	Energy	Hodograph	Improved
3	0.33 s	0.118 s	0.124 s
10	1.19 s	0.148 s	0.135 s
17	3.12 s	0.156 s	0.160 s
24	6.87 s	0.181 s	0.167 s
30	11.5 s	0.209 s	0.181 s
37	20.3 s	0.217 s	0.195 s
44	32.3 s	0.236 s	0.209 s
50	46.5 s	0.255 s	0.222 s

Table 1. Tabulated computation times.

Computation Time

The computation time required for each algorithm to perform 3000 Monte Carlo runs is tabulated in Table 1 and shown in Figure 3. The hodograph method and the improved method are similar and significantly faster than the energy method. Interestingly, the improved method is faster when parsing many measurements, despite having an iterative circle fit algorithm as compared to the non-iterative hodograph method.

Choice of Algorithm

The improved method outperforms previous VIOD methods both in terms of accuracy and computation speed, making it the clear candidate for further analysis among the three methods presented. In the next chapter, the improved method will be analyzed in greater depth, and an analytic error model will be developed.

ERROR MODELING FOR THE IMPROVED HODOGRAPH METHOD

Since the improved hodograph method is based upon fitting velocity measurements to the orbit hodograph, it reasons that analyzing the orbit hodograph can reveal mechanisms by which VIOD error develops. This section of the paper identifies these mechanisms and analytically models their impact on the circle fitting error, E . A critical assumption is then made, that the circle fitting error is proportional to VIOD error:

$$E \propto \epsilon \quad (42)$$

A key point to reiterate is that the models developed henceforth only model the proportionality between VIOD error and aspects of the hodograph, so only the trend of VIOD error can be derived, but not a numeric value for any particular case.

Error Modeling: Velocity and Noise

An intuitive mechanism for VIOD error is the ratio between noise and velocity. For the same velocity measurements, greater noise increases error. Conversely, for the same noise, greater velocity measurements reduce error. The noise-to-velocity ratio (NVR), therefore, can be related to the hodograph circle fitting error. To examine this relationship, define NVR as follows:

$$NVR = \frac{\sigma}{R} \quad (43)$$

where σ is the sensor noise standard deviation and R is the radius of the hodograph. 3000-run Monte Carlo simulations were performed for a broad range of NVR values in several orbit configurations, whose results are shown in Figure 4.

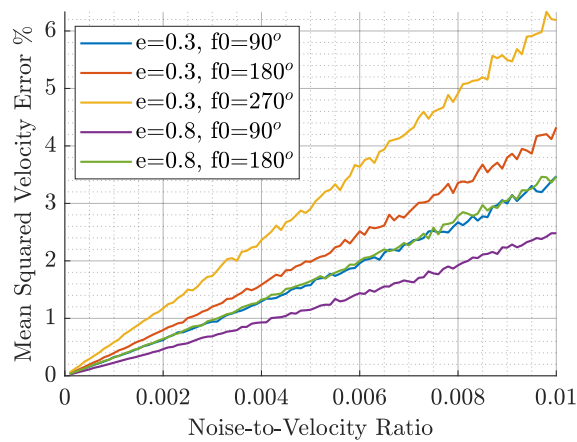


Figure 4. The hodograph circle fit error is linear with respect to NVR.

It is clear that regardless of orbit configuration, the relation between NVR and circle fitting error is linear: $NVR \propto E$. Combining with the assumption made earlier in the section from Eq. (42) yields the relation between NVR and VIOD error:

$$NVR \propto \epsilon \quad (44)$$

Error Modeling: Eccentricity

With all other parameters unchanged, varying the eccentricity can affect the size of the hodograph, i.e. the magnitude of the velocity measurements. Specifically, one can calculate the hodograph radius by expressing the velocity at periapsis and apoapsis, thus obtaining the equation for hodograph radius with respect to eccentricity in Eq. (47).

$$v_p = \sqrt{\frac{\mu}{a} \cdot \frac{1+e}{1-e}} \quad (45)$$

$$v_a = \sqrt{\frac{\mu}{a} \cdot \frac{1-e}{1+e}} \quad (46)$$

$$R = \frac{1}{2} (v_p + v_a) = \frac{1}{2} \sqrt{\frac{\mu}{a}} \left(\sqrt{\frac{1+e}{1-e}} + \sqrt{\frac{1-e}{1+e}} \right) \quad (47)$$

Combining Eq. (47) with Eqs. (43) and (44) then yields the relation between eccentricity and ϵ :

$$\epsilon \propto \left(\sqrt{\frac{1+e}{1-e}} + \sqrt{\frac{1-e}{1+e}} \right)^{-1} \quad (48)$$

From Eq. (48), it is clear that a higher eccentricity would produce a larger hodograph. This effect is illustrated in Figure 5, where three velocity measurements are taken at equal time intervals for three orbits with different eccentricities but the same orbit period.

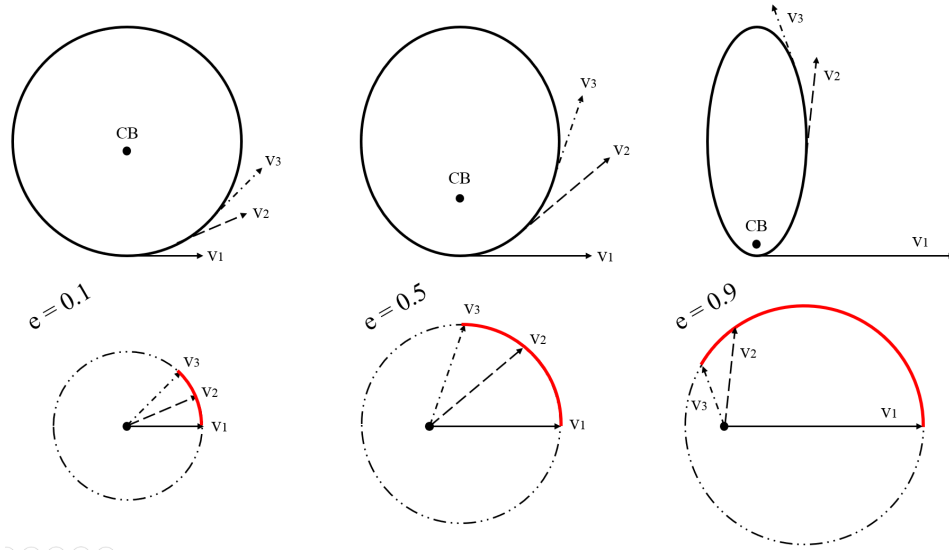


Figure 5. Increasing eccentricity of the orbit causes the hodograph size to increase.

Error Modeling: True Anomaly Span

Changes in the true anomaly spanned by velocity measurements affect the portion of the hodograph supplied to the circle fitting algorithm, which in turn impacts VIOD accuracy. The true anomaly span can be altered by changing any of the following three parameters: measurement duration, starting true anomaly, or eccentricity. Figure 5 illustrates how changing eccentricity can affect the true anomaly span. Figure 6 demonstrates the changes caused by different starting true anomalies. A simple analysis shows how these parameters influence Δf analytically.

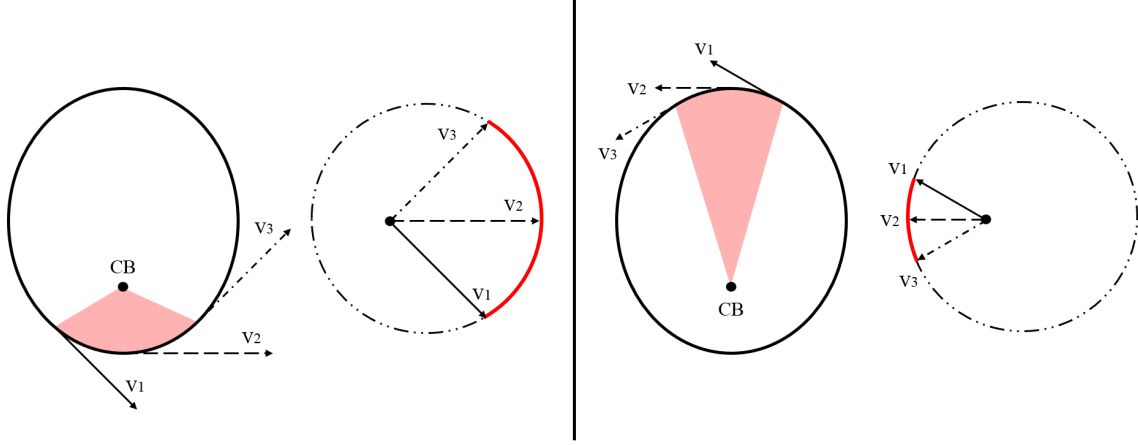


Figure 6. Over the same total time (pink), measurements taken near periapsis (left) are span a greater portion of the hodograph as compared to measurements taken near apoapsis (right).

Assume n velocity measurements are taken at equal time intervals T in an orbit with semi-major axis a , eccentricity e , and starting true anomaly f_0 about a central body with gravitational parameter μ . To determine the true anomaly spanned by these measurements, begin by finding the starting mean anomaly, M_0 :

$$E_0 = 2 \arctan \left[\sqrt{\frac{1-e}{1+e}} \tan \left(\frac{f_0}{2} \right) \right] \quad (49)$$

$$M_0 = E_0 - e \sin E_0 \quad (50)$$

The ending mean anomaly can then be calculated:

$$M_e = M_0 + \frac{(n-1)T}{2\pi} \sqrt{\frac{\mu}{a^3}} \quad (51)$$

Finally, the ending eccentric anomaly can be determined by solving Kepler's equation in Eq. (52) using Newton's method, and the true anomaly span can be recovered using Eqs. (53)-(54).

$$M_e = E_e - e \sin E_e \quad (52)$$

$$f_e = 2 \arctan \left[\sqrt{\frac{1+e}{1-e}} \tan \left(\frac{E_e}{2} \right) \right] \quad (53)$$

$$\Delta f = f_e - f_0 \quad (54)$$

Proceeding, simulations were performed to determine the relation between Δf and ϵ . The results are shown in Figure 7, and the relation is expressed in Eq. (55).

$$\epsilon \propto (\Delta f)^{-2} \quad (55)$$

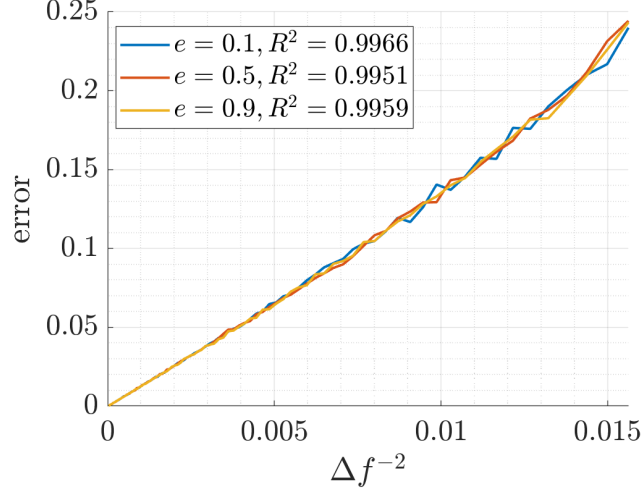


Figure 7. The hodograph circle fit error is linear with respect to the inverse square of true anomaly span, Δf . Simulated Δf values range from 8° to 350° .

Error Modeling: SVD

Another factor impacting VIOD accuracy is the error derived from SVD. Recall that SVD is used to define the orbit plane normal \mathbf{k} . Intuitively, a greater NVR would decrease the quality of the orbit plane normal found from SVD, thus increasing VIOD error. The impact of SVD error was not determined analytically, but instead evaluated using Monte Carlo simulations. The unit vector \mathbf{k} that defines the normal of the orbit plane is first found using ground truth velocity data. Then, Gaussian noise is applied to the velocity data, which is then used to estimate the orbit plane normal, $\tilde{\mathbf{k}}$. The relative error is computed over n Monte Carlo runs to obtain the root mean squared orbit plane error: ϵ_{svd} .

$$\epsilon_{svd} = \sqrt{\frac{1}{n} \sum_{j=1}^n \left(\frac{\|\mathbf{k} - \tilde{\mathbf{k}}_i\|}{\|\mathbf{k}\|} \right)^2} \quad (56)$$

ERROR MODEL VERIFICATION

The analytic models derived in the previous chapter are now verified against Monte Carlo simulations. The VIOD error, ϵ , will be assessed over variations mission parameters and sensor parameters.

Mission parameters include the semi-major axis, eccentricity, starting true anomaly of the orbit. These parameters represent intrinsic, mission-specific factors that cannot be controlled/modified to improve VIOD. Sensor parameters include the sensor noise, measurement duration, and number of measurements. These parameters represent variables that can be controlled/modified to obtain greater results from VIOD, independently of the mission.

Note once again that the models developed above only reflect proportionality, but do not generate exact error values, and hence can only be used to predict error trends. The predicted errors presented in the remainder of this section were scaled and offset to match the lower and upper bounds of the simulation data. Nonetheless, as the results will show, the analytic models are able to model error trends adequately.

Verification: Semi-Major Axis

To establish the relation between the semi-major axis a and the VIOD error, observe from Eq. (47) that R is proportional to $a^{-1/2}$:

$$R = \frac{1}{2} (v_p + v_a) = \frac{1}{2} \sqrt{\frac{\mu}{a}} \left(\sqrt{\frac{1+e}{1-e}} + \sqrt{\frac{1-e}{1+e}} \right) \quad (47)$$

$$R \propto a^{-1/2} \quad (57)$$

Relating Eq. (57) to Eqs. (43) and (44) with a fixed σ , obtain

$$\epsilon \propto \sqrt{a} \quad (58)$$

A 3000-run Monte Carlo simulation with $e = 0.5$, $f_0 = 90^\circ$, $\sigma = 3 \times 10^{-6} \text{ DU/TU}$ was performed with 10 measurements over 10% of the orbit period for semi-major axis lengths between 1×10^4 and $1 \times 10^6 \text{ DU}$. As shown in Figure 8, the analytic model matches perfectly with the simulation results.

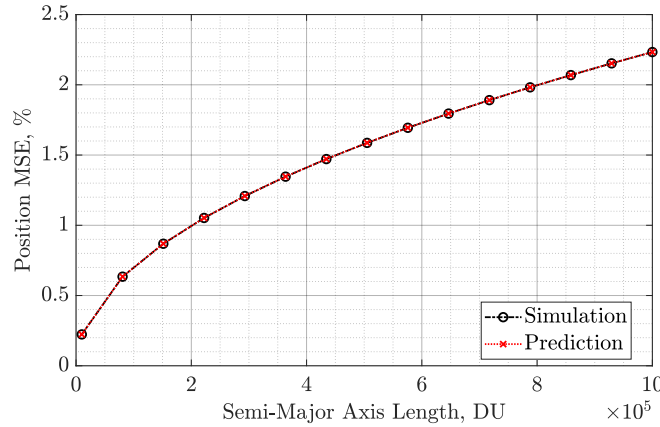


Figure 8. The analytic model in Eq. (58) perfectly matches Monte Carlo simulations.

Verification: Eccentricity

As discussed in previous subsections, changes in the eccentricity of the orbit can affect VIOD error by changing the size of the hodograph and the true anomaly span. Their combined effect is shown in Eq. (59). In Figure 9, the error model is compared against Monte Carlo simulations at multiple true anomalies, and yields similar results.

$$\epsilon \propto (\Delta f)^{-2} \left(\sqrt{\frac{1-e}{1+e}} + \sqrt{\frac{1+e}{1-e}} \right)^{-1} \quad (59)$$

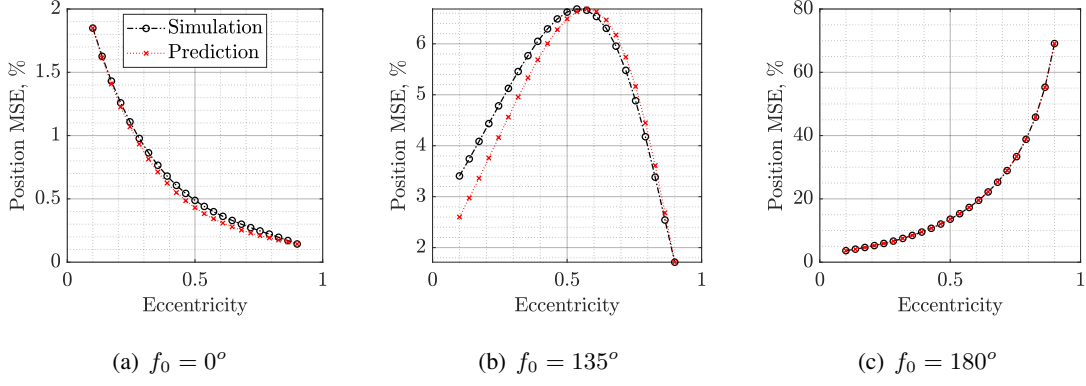


Figure 9. The predicted error trend with respect to eccentricity change closely matches simulated results for multiple starting true anomalies.

Verification: True Anomaly

Varying the starting true anomaly alters the true anomaly span of the measurements, thus changing VIOD error. This effect is shown in Eq. (60). In Figure 10, the error model is compared against Monte Carlo simulations at multiple eccentricities, and yields nearly identical results.

$$\epsilon \propto (\Delta f)^{-2} \quad (60)$$

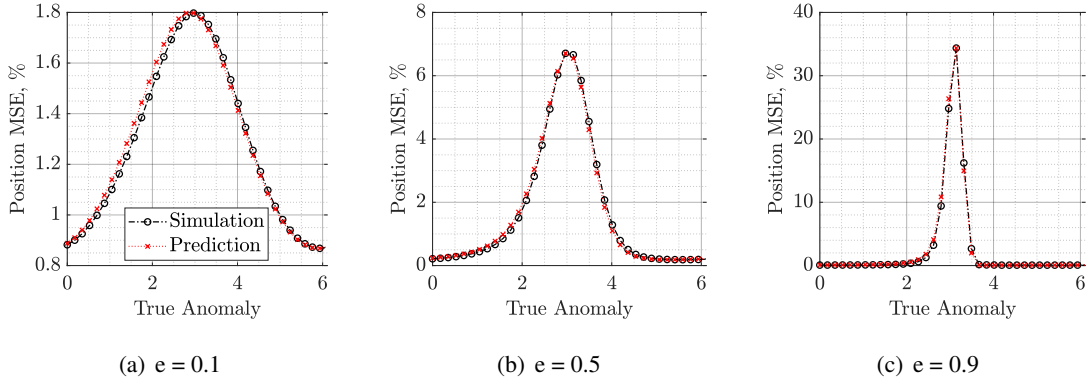


Figure 10. The predicted error trend with respect to starting true anomaly change closely matches simulated results for multiple eccentricities.

Verification: Sensor Noise

It is clear from Eqs. (43) and (44) that if the orbit is not changed, the VIOD error and sensor noise can be related by the following:

$$\epsilon \propto \sigma \quad (61)$$

A 3000-run Monte Carlo simulation with $a = 1 \times 10^5$ DU, $e = 0.5$, $f_0 = 90^\circ$, was performed with 10 measurements over 10% of the orbit period for sensor noise standard deviation σ between

5×10^{-7} and $1 \times 10^{-5} \text{ DU/TU}$. As shown in Figure 11, the analytic model matches closely with the simulation results.

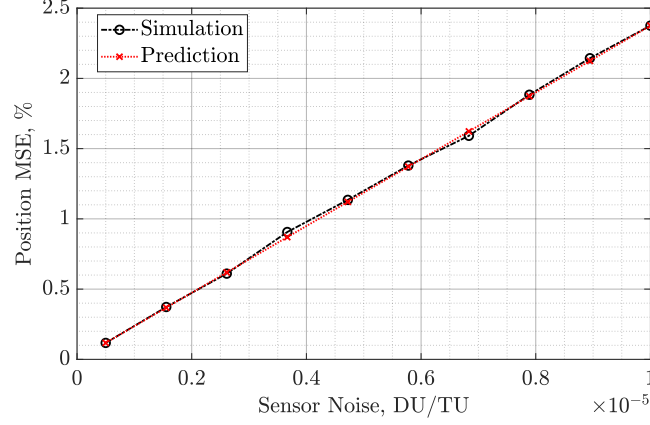


Figure 11. The analytic model in Eq. (61) closely matches Monte Carlo simulations, showing that VIOD error is linear with respect to sensor noise.

Verification: Measurement Duration

Intuitively, increasing measurement duration increases the true anomaly spanned, and according to Eq. (55) should decrease VIOD error. However, in certain cases increasing measurement time causes velocity measurements to decrease in magnitude sufficiently to overcome the benefits of having increased Δf . The overall relation between measurement duration and VIOD error is then the following:

$$\epsilon \propto \epsilon_{svd} (\Delta f)^{-2} \quad (62)$$

Figure 12 shows the analytic model matching Monte Carlo simulation results in several orbit configurations. Note how in Figure 12(c) the VIOD error increases with more measurement time, due to the mechanism described above.

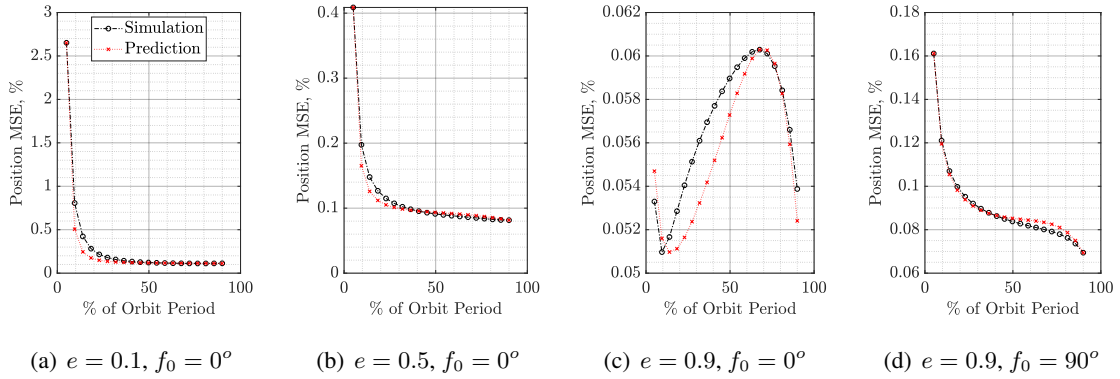


Figure 12. The analytic model in Eq. 62 closely matches simulation data for a wide range of orbits, and successfully predicts an error increase in the highly eccentric case.

Verification: Number of Measurements

Increasing the number of measurements does not change the true anomaly span or size of the hodograph. Its only impact comes from the reduced uncertainty caused by a larger sample size, and SVD error. Therefore the relation between the number of measurements and VIOD error is simply modeled by Eq. (62). A comparison between the analytic model and Monte Carlo simulation results is shown in Figure 13, showing that the error behavior is generally predicted correctly.

$$\epsilon \propto \epsilon_{svd} \quad (63)$$

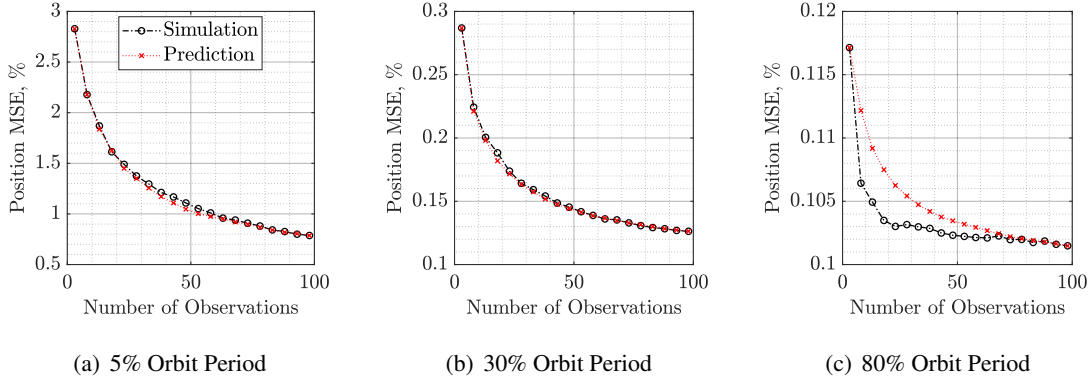


Figure 13. The analytic model from Eq. (62) is able to capture the general error trend with respect to an increase in the number of observations.

CONCLUSION

An improved VIOD algorithm was proposed and demonstrated to be more accurate and computationally efficient than previous VIOD algorithms. With the improved algorithm, VIOD performance was successfully modeled by using the orbit hodograph to relate changes in mission and sensor parameters with position error. Analytic relations were established between VIOD error and each parameter, then validated against Monte Carlo simulation results.

A significant drawback to the current error model is that it can only predict VIOD error trends using the proportionality between VIOD error and each parameter. It does not have the capability of producing numerical error predictions given a particular orbit and spacecraft configuration. Future studies that can determine the exact analytic relation would significantly improve the practicality of using the analytic error model to predict VIOD error.

REFERENCES

- [1] J. A. Christian and C. L. Hollenberg, "Initial orbit determination from three velocity vectors," *Journal of Guidance, Control, and Dynamics*, Vol. 42, No. 4, 2019, 10.2514/1.G003988.
- [2] C. L. Hollenberg and J. A. Christian, "Geometric Solutions for Problems in Velocity-Based Orbit Determination," *Journal of the Astronautical Sciences*, Vol. 67, mar 2020, 10.1007/s40295-019-00170-7.
- [3] J. Prussing and B. Conway, *Orbital Mechanics*. Oxford University Press, 2012.
- [4] J. Branham, R. L., "Laplacian Orbit Determination," *Astronomy in Latin America* (R. Teixeira, N. V. Leister, V. A. F. Martin, and P. Benevides-Soares, eds.), Vol. 1, Nov. 2003.

- [5] L. G. Taff, "On Initial Orbit Determination," *The Astronomical Journal*, Vol. 89, Sept. 1984, 10.1086/113644.
- [6] H. D. Curtis, "Chapter 5 - Preliminary Orbit Determination," *Orbital Mechanics for Engineering Students (Second Edition)*, pp. 255 – 317, Boston: Butterworth-Heinemann, 2010.
- [7] R. Gooding, "A new procedure for orbit determination based on three lines of sight (angles only)," tech. rep., Defence Research Agency Farnborough (United Kingdom), 1993.
- [8] S. I. Sheikh, D. J. Pines, P. S. Ray, K. S. Wood, M. N. Lovellette, and M. T. Wolff, "Spacecraft navigation using X-ray pulsars," *Journal of Guidance, Control, and Dynamics*, Vol. 29, No. 1, 2006.
- [9] J. Mitchel, L. Winternitz, M. Hassouneh, S. Price, S. Semper, W. Yu, P. Ray, M. T. Wolff, M. Kerr, K. S. Wood, *et al.*, "SEXTANT X-ray pulsar navigation demonstration: initial on-orbit results," 2018.
- [10] L. B. Winternitz, M. A. Hassouneh, J. W. Mitchell, S. R. Price, W. H. Yu, S. R. Semper, P. S. Ray, K. S. Wood, Z. Arzoumanian, and K. C. Gendreau, "SEXTANT X-ray pulsar navigation demonstration: additional on-orbit results," *2018 SpaceOps Conference*, 2018, p. 2538.
- [11] L. M. B. Winternitz, J. W. Mitchell, M. A. Hassouneh, J. E. Valdez, S. R. Price, S. R. Semper, W. H. Yu, P. S. Ray, K. S. Wood, Z. Arzoumanian, and K. C. Gendreau, "SEXTANT X-ray Pulsar Navigation demonstration: Flight system and test results," *2016 IEEE Aerospace Conference*, 2016, pp. 1–11.
- [12] A. Al-Sharadqah and N. Chernov, "Error analysis for circle fitting algorithms," *Electronic Journal of Statistics*, Vol. 3, 2009, 10.1214/09-EJS419.
- [13] N. Chernov and C. Lesort, "Least Squares Fitting of Circles," *Journal of Mathematical Imaging and Vision*, Vol. 23, 2005, 10.1007/s10851-005-0482-8.
- [14] S. Eliassi, "GitHub - Circle-Fitting-Hyper-Fit," 2017. <https://github.com/SohranEliassi/Circle-Fitting-Hyper-Fit>, Last accessed on 2020-08-06.